Crowding and queuing at exits and bottlenecks

Michael Fischer, Gaspard Jankowiak, Marie-Therese Wolfram

CROWDING AND QUEUING AT EXITS AND BOTTLENECKS

FISCHER MICHAEL, JANKOWIAK GASPARD, AND WOLFRAM MARIE-THERESE

Abstract. Experiments with pedestrians revealed that the geometry of the domain, as well as the incentive of pedestrians to reach a target as fast as possible have a strong influence on the overall dynamics. In this paper we propose and validate different mathematical models on the micro- and macroscopic level to study the influence of both effects. We calibrate the models with experimental data and compare the results on the micro- as well as macroscopic level. Our numerical simulations reproduce qualitative experimental features on both levels and indicate how geometry and motivation level influence the observed pedestrian density. Furthermore, we discuss the dynamics of solutions for different modeling approaches and comment on the analysis of the respective equations.

1. Introduction

In this paper we develop and analyze mathematical models for crowding and queuing at exits and bottlenecks, which are motivated by experiments conducted at the Forschungszentrum Jülich and the University of Wuppertal, see [3]. In these experiments student groups of different size were asked to exit through a door as fast as possible. In each run the geometry of the domain, ranging from a narrow corridor to an open space, as well as the motivation level, by giving more or less motivating instructions, were varied. The authors observed that

- The narrower the corridor, the more people people lined up. This led to a significantly lower pedestrian density in front of the exit.
- A higher motivation level led to an increase of the observed densities. However its impact on the density was smaller than changing the shape of the domain.

Adrian et al. [3] supported their results by a statistical analysis of the observed data as well as computational experiments using a force based model. We follow a different modeling approach in this paper, proposing and analyzing a cellular automaton (CA) model which is motivated by the aforementioned experiments. We see that these minimalistic mathematical models reproduce the observed behavior on the microscopic as well as macroscopic level very well.

There is a rich literature on mathematical models for pedestrian dynamics. Ranging from microscopic agent or cellular automaton based approaches to the macroscopic description using partial differential equations. The social force model, see [16], is the most prominent individual based model. Here pedestrians are characterized by their position and velocity, which change due to interactions with others and their environment. More recently, the corresponding damped formulation, see [3], has been considered in the literature. In cellular automata (CA), another much used approach, individuals move with given rates from one discrete cell to another. One advantage of CA approaches is that the formal passage from the microscopic to the macroscopic level is rather straight-forward based on a Taylor expansion of the respective transition rates. This can for example be done systematically

using tools from symbolic computation, see [21]. CA approaches have been used successfully to describe lane formation, as for example in [29], or evacuation situations, such as in [20]. The dynamics of the respective macroscopic models was investigated in various situations such as uni- and bidirectional flows or cross sections, see for example [6, 7]. Macroscopic models for pedestrian dynamics are usually based on conservation laws, in which the average velocity of the crowd is reduced due to interactions with others, see [30, 35]. In general it is assumed that the average speed changes with the average pedestrian density, a relation known as the fundamental diagram. In this context, finite volume effects, which ensure that the maximum pedestrian density does not exceed a certain physical bound, play an important role. These effects result in nonlinear diffusivities, which saturate as the pedestrian density reaches the maximum density, and cross-diffusion in case of multiple species, see for example [6]. One of the most prominent macroscopic models is the Hughes model, see [12, 17]. It consists of a nonlinear conservation law for the pedestrian density which is coupled to the eikonal equation to determine the shortest path to a target (weighted by the pedestrian density). We refer to the textbooks by Cristiani et al., see [11] and Maury and Favre, see [27], for a more detailed overview on pedestrian dynamics.

Many PDE models for pedestrian dynamics can be interpreted as formal gradient flows with respect to the Wasserstein distance. In this context, entropy methods have been used successfully to analyze the dynamics of such equations. For example, the boundedness by entropy principle ensures the global in time existence of weak solutions for large classes of nonlinear partial differential equation systems, see [19]. These methods have been proven to be useful also in the case of nonlinear boundary conditions. For example Burger and Pietschmann [7] proved existence of stationary solutions to a nonlinear PDE with nonlinear inflow and outflow conditions, modeling unidirectional flows in corridors, using entropy techniques. The respective time dependent result was subsequentially presented in [14].

The calibration of microscopic pedestrian models is of particular interest in the engineering community. Different calibration techniques have been used for the social force model, see [18, 28] and CA approaches, see [33, 34]. A large number of datasets are publicly available - for example the database containing data for a multitude of experimental setups at the Forschungszentrum in Jülich, or data collected in a Dutch railway stations over the course of one year, see [10]. However, many mathematical questions concerning the calibration of macroscopic and mean-field models from individual trajectories are still open.

In this paper we develop and analyze mathematical models to describe queuing individuals at exits and bottlenecks. Our main contributions are as follows:

- Develop microscopic and macroscopic models to describe pedestrian groups with different motivation levels and analyze their dynamics for various geometries.
- Calibrate and validate the microscopic model with experimental data in various situations.
- Compare the dynamics across scales using computational experiments.
- Present computational results, which reproduce the experimentally observed characteristic behavior.

This paper is organized as follows. We discuss the experimental setup and the proposed CA approach in Section 2. In Section 3 we present the details of the corresponding CA implementation and use experimental data to calibrate it. Section 4 focuses on the description on the macroscopic level by analyzing the solutions to the corresponding formally

derived PDE. We conclude by discussing alternative modeling approaches in Section 5 and summaries our findings in Section 6.

2. The experimental setup and the microscopic model

2.1. **The experimental setup.** We start by discussing the experiments, which serve as the motivation for the proposed microscopic model, see [3]. These experiments were conducted at the University of Wuppertal, Germany. The respective data is available online, see [1].

The conducted experiments were designed to obtain a better understanding how social cues and the geometry of the domain influence individual behavior. For this purpose runs with five different corridor widths, varying from 1.2 to 5.6m, were conducted over the course of several days. For each corridor a group of students was instructed to reach a target. These runs were then repeated with varying instructions, for example suggesting that queuing is known to be more efficient or suggesting to go as fast as possible. The instructions were given to vary the motivation level and see their effect on the crowd dynamics. The number of students in the different runs (which corresponded to the different corridor width) varied from 20 to 75. The trajectory of each individual was recorded and used to compute the average density with the software package JuPedSim, available at [2]. The post-processed data showed that the average pedestrian density becomes particularly high in a 0.8 times 0.8 meter area, 0.5 meters in front of the exit, highlighted in Figure 1a. Within this area average densities up to 10 p/m^2 (pedestrians per square meter) were observed. The densities varied significantly for the different runs - they were much lower for corridor-like domains and increased with the motivation level. Further details on the experimental setup can be found in [3].

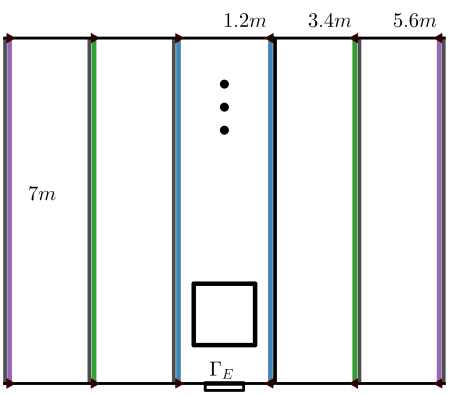

(A) Sketch of experimental setup at the University of Wuppertal, showing the different corridor width, the exit Γ_E and the measurement area.

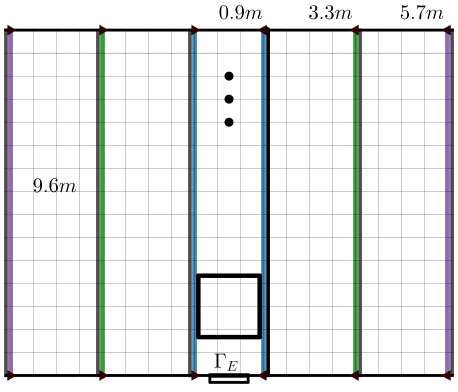

(B) Computational domain with adapted width to ensure a consistent discretization of the exit.

FIGURE 1. Comparison of the experimental setup and the computational domain.

2.2. **The cellular automaton approach.** In the following we introduce a cellular automaton approach to describe the dynamics of agents queuing in front of the bottleneck. The dynamics of agents is determined by transition rates, which depend on the individual motivation level and the distance to the target.

We split the domain into squared cells with side length $\Delta x = 0.3$m which corresponds to a maximum packing density of 11.11 p/m^2. Cell-sizes of 0.09m^2 have a comparable area as ellipses with semi-axes $a = 0.23$m and $b = 0.12$m - a reference measure for pedestrians commonly used in agent based simulations, see [15]. The cellular automaton is implemented on a Moore neighborhood, see Figure 2a. Agents are allowed to move into the eight neighboring sites. Their transition rates depend on the availability of a site – a site can only be occupied by a single agent at a time – the potential ϕ, which corresponds to the minimal distance to the exit, as well as the individual motivation level. The positions of all agents are updated simultaneously, a so-called parallel update. In doing so, we calculate the transition rates for every agent and resolve possible conflicts. In case of a conflict the respective probabilities of the two agents wanting to move into the site are re-weighted, and one of them is selected. This solution has been proposed by [8, 20] and is illustrated in Figure 2b.

Particular care has to be taken when modeling the exit. Consider a Markov-process, in which a single agent is located at distance Δx to the exit, see Figure 3a. We see that the exit can stretch over two or three cells, both cases have different exit probabilities and influence the exit rate. Figure 3b illustrates the different exit rates for the two situations in case of a single agent. We observe that the exit rate is higher if the exit is discretized using two cells. To ensure a consistent discretization of the exit for all corridor widths, we choose a discretization using three cells for all corridors. Therefore, we changed the respective corridor widths in the presented computational experiments to 0.9m, 3.3m and 5.7m, as illustrated in Figure 1. Furthermore, we extended the corridor to 9.6m to ensure sufficient space for all agents in case of larger groups. Note that in the actual experiments individuals were waiting behind the corridor entrance.

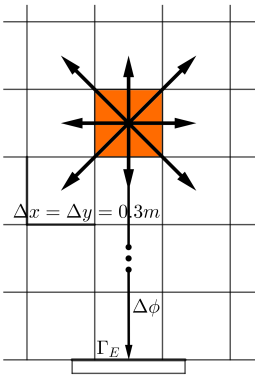

(A) Moore neighborhood; the potential ϕ corresponds to the distance to the exit.

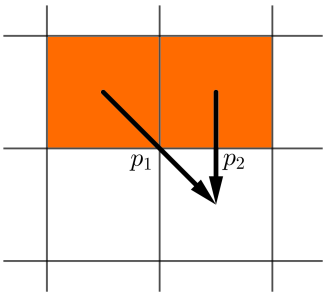

(B) Conflict: Agent 1 wins with probability $\tilde{p}_1 = p_1/(p_1 + p_2)$, agent 2 with probability $1 - p_1$.

FIGURE 2. Cellular automaton: transition rules.

Transition-rates and the master equation. The transition rates are based on the following assumptions, which are motivated by the previously detailed experiments:

- Individuals want to reach a target as fast as possible.
- They can only move into a neighboring site if it is not occupied.
- The higher the motivation level, the larger the transition rate.

Let $\rho = \rho(x, y, t)$ denote the probability of finding an individual at site (x, y) at time t and μ correspond to the motivation level. We state only one transition rate in the following,

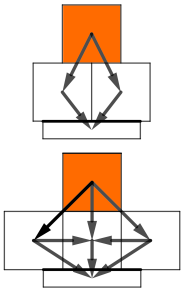

(A) Two vs. three cells.

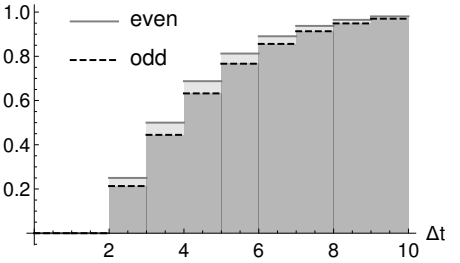

(B) Two vs. three: comparison of the exit rate as a function of time.

FIGURE 3. Discretization of the exit. In the case of an even number of cells, a central positioned agent will leave the corridor faster than in the case of three cells.

since all other rates have the same structure with the obvious modifications.
The transition-rate $\mathcal{T}$ of an agent located at position (x, y) to move to the right, that is to $(x + \Delta x, y)$ is given by

$$\begin{aligned}\mathcal{T}^{(x,y)\to(x+\Delta x,y)} &:= \mathcal{T}^{+0}(x, y)\\ &= (1 - \rho(x + \Delta x, y, t))\frac{1}{8(3-\mu)} \exp\left(\beta(\phi(x, y) - \phi(x + \Delta x, y))\right).\end{aligned} \tag{1}$$

Here the factor $(1 - \rho(x + \Delta x, y, t))$ ensures that the target site is not occupied, the prefactor $\frac{1}{8}$ is a scaling constant such that $\sum_i \mathcal{T}^i = 1 + \mathcal{O}((\Delta x)^2)$ holds. The prefactor $(3 - \mu)$ changes the transition rate depending on the motivation level $\mu \in (-\infty, 3)$. It also ensures that it is very unlikely that individuals step back as β increases. The rates increase in direction where the potential ϕ decreases. Hence individuals are more likely to move towards the exit.
Then the probability that (x, y) is occupied at time $t+\Delta t$, is given by the so-called master equation

$$\begin{aligned}\rho(x, y, t + \Delta t) =&\rho(t, x, y) - \rho(x, y, t) \sum_{(i,j)\in I} \mathcal{T}^{ij}(x, y)\\ &+ \sum_{(i,j)\in I} \rho(x + i\Delta x, y + j\Delta x, t)\mathcal{T}^{ij}(x + i\Delta x, y + j\Delta x),\end{aligned} \tag{2}$$

where the set $I := \{-1, 0, +1\}^2 \setminus \{(0, 0)\}$ corresponds to the Moore neighborhood of the respective sites.
We recall that agents can leave the domain from all three fields in front of the exit. In a possible conflict situation, that is two or three agents located in the exit cells want to leave simultaneously, the conflict situation is resolved and the winner exists with probability p_{ex}.

Remark 2.1. The choice of a Moore neighborhood instead of a Neumann neighborhood (as in [29, 37]), is based on the experimental observations (individuals make diagonal moves to get closer to the target). Note that the choice of the neighborhood does not change the structure of the limiting partial differential equation.

Remark 2.2. With the proposed scaling, a motivated agent, which corresponds to $\mu = 1$, jumps every second time-step since $\mathcal{T}^{00} = 1 - \sum_{i,j\in I} \mathcal{T}^{ij}(x, y) = \frac{2-\mu}{3-\mu}$. Note that the motivation μ has a direct influence on the desired maximum velocity v_{max}.

3. Validation and calibration of the CA model

3.1. **Implementation of the CA approach.** We start by briefly discussing the implementation of the CA, which will be used for the calibration in the subsequent section. A CA simulation returns the average exit time (that is the time when the last agent leaves the corridor) depending on the number of agents n, the corridor-width $w \in \{0.9, 3.3, 5.7\}$, the motivation μ, the length of a time-step Δt and the parameter β. Each CA simulation is initialized with a random uniform distribution of agents. For given parameters the returned average exit time $\bar{T}$ and maximum observed density is estimated by averaging over 5000 CA simulations. Note that we calculate this density in the area highlighted in Figure 1a.
We check the consistency of the estimated average exit time by varying the number of MC simulations. We observe that the distribution of the exit time converges to a unimodal curve, see Figure 4c. Similar results are obtained across a large range of parameter combinations.

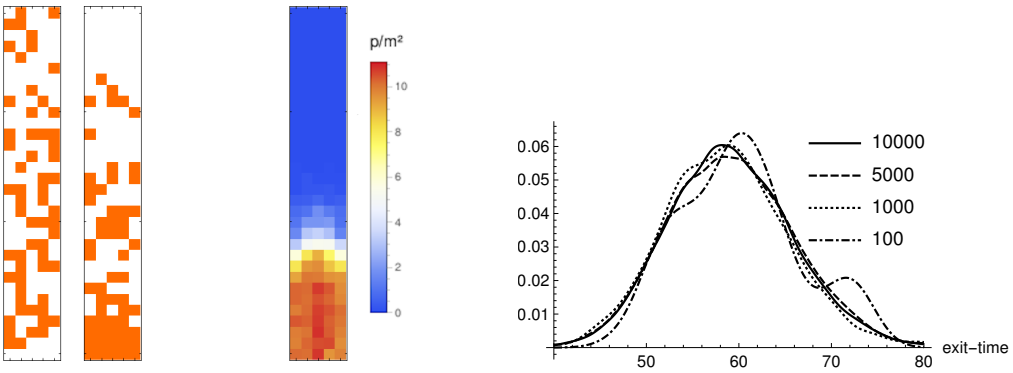

(A) Distribution of $n = 40$ agents at time $t = 0$ and $t = 16\Delta t$.

(B) The simulated density.

(C) Densities of exit times when increasing the number of MC runs.

FIGURE 4. Solutions of the CA approach.

3.2. **Calibration.** In this Section we discuss a possible calibration of the developed CA approach using the experimental data available, see [1]. We wish to identify the parameter scaling parameter β, the timestep Δt and the exit rate p_{ex}. In doing so we make the following assumptions:

- The outflow rate p_{ex} does not depend on the motivation level and the corridor width.
- There is a one-to-one relation between the parameter β and the time step Δt.

We start by considering the dynamics of a single agent in the corridor. These dynamics, although not including any interactions, give first insights and provide reference values for the calibration. Velocities of pedestrians are often assumed to be Gaussian distributed. Different values for the mean and variance can be found in the literature, see for example [13, 36]. We set the desired maximum velocity of a single agent to $v_{max} = 1.2\frac{m}{s}$, as for example in [13]. Hence a single motivated agent, having motivation level $\mu = 1$, needs approximately 8 seconds to travel the 9.6m long corridor.

Let $\bar{N}$ denote the average number of time steps to the exit. We will see in the following that there is a one to one relationship between the scaling parameter β and the exit time, which allows us to estimate the time step Δt.
Figure 5a illustrates the dynamics of this single agent for different values of β – we see that the larger β, the straighter the path to the exit. We observe that the average number of time steps $\bar{N}$ to the exit of an agent starting at the same position converges as β increases, see Figure 5b. The observed relation between the exit time and the value of β in Figure 5b

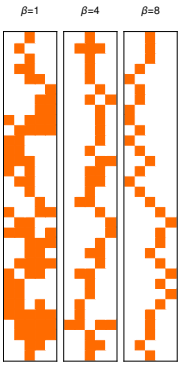

(A) Trajectories for different β - increasing β reduces the randomness of the walk.

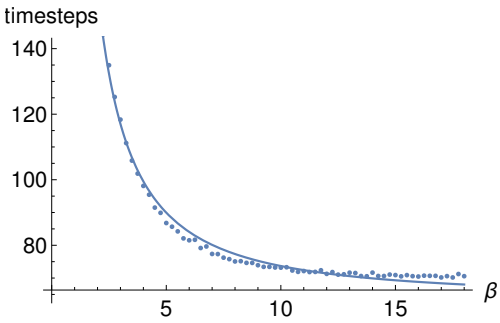

(B) $\bar{N}$ for different values of β. The dots mark experimental data, the curve is that of the relation (3).

FIGURE 5. Influence of the scaling parameter β on individual dynamics.

can be estimated by a function of the form

$$\bar{N}(\beta, p_{ex} = 1.1) = 63.528 + \frac{244.082}{\beta^{1.38148}}, \tag{3}$$

which was computed using a least square-approach for $a + \frac{b}{\beta^c}$. The functional relation captures the asymptotic behavior correctly (converging to the minimum number of steps going straight to the exit) and the sharp increase for small β.
This asymptotic relation allows us to estimate the time steps Δt for a given value of β in case of a single agent. Since a motivated agent moves on average every second step, it needs approximately 64 steps to exit the corridor, which corresponds to 32 vertical fields. A somehow similar approach was proposed in [37], where the position of agents was updated according to the individual velocity.
We will now estimate the missing two parameters β and p_{ex} using three different data sets, see Table 1. We restrict ourselves to these three datasets, since the number of individuals in each run is similar and their initial distribution is close to uniform, fitting the initial conditions of the CA simulations best. For each run we use the respective modified corridor width w, to ensure a consistent discretization of the exit and the number of agents n as detailed in Table 1.
Reference values: We use the experimental data to obtain reference values for β and p_{ex}. For p_{ex} we use all data sets available, that is a total number of 980 trajectories recorded for corridors of different widths and consider the respective exit times. This gives a first approximation $p_{ex} = 1.1\frac{p}{s}$, which we use as a reference value for the calibration later on. A similar value for p_{ex} was reported in [15]. We will allow for estimates within a 50%

Run	$\mu = 1$	μ_0
01, $n = 1$	$8s$	
02, $n = 63, w = 1.2m$	$53s$	$64s$
03, $n = 67, w = 3.4m$	$60s$	$68s$
04, $n = 57, w = 5.6m$	$55s$	$57s$

TABLE 1. exit times for different runs and different motivations from [3]. Run 01 is used to set the desired maximum velocity v_{max}.

deviation from that value. Furthermore we restrict β to $[0.5, 10]$ (motivated by the observations in Figure 5a).

The calibration is then based on minimizing the difference between the observed exit time and the computed average exit time $\bar{T}$. We define the the average exit time

$$\bar{T} = \bar{T}(\beta, p_{ex}, \Delta t, \mu, n, w) : [0, \infty) \times \mathbb{R}^+ \times \mathbb{R}^+ \times (-\infty, 1] \times \mathbb{N} \times \{0.9, 3.3, 5.7\} \to \mathbb{R}^+ ,$$

that is the time needed for the last agent to leave the domain, for n individuals in a corridor of width w and parameters β, p_{ex}, Δt and μ. The calibration is then based on minimizing the functional

$$\begin{aligned} \mathcal{T} = \Big(& (\bar{T}(\beta, p_{ex}, 63, \Delta t, 0.9) - 53)^2 + (\bar{T}(\beta, p_{ex}, 67, \Delta t, 3.3) - 60)^2 \\ & + (\bar{T}(\beta, p_{ex}, 57, \Delta t, 5.7) - 55)^2 \Big)^{0.5}, \end{aligned} \tag{4}$$

using the data stated in Table 1. The functional $\mathcal{T}$ is not differentiable, hence we used derivative free methods to find a minimum. We first used a parallel Nelder-Mead, which did not converge. We believe that this is caused by the stochasticity of the problem (since we average over 5000 MC runs to compute the average exit time) as well as the form of the functional itself. Similar problems were reported in [32]. Systematic computational experiments show that the parameter β has a small influence on the exit time. In narrow corridors, increasing the value of β does not improve the exit time, since the geometry restricts the range of jumps. In wider corridors, β plays a more important role. However, we have seen that the exit time for a single agent converges as β increases. Therefore we can not expect a unique single optimal value. Furthermore we believe that the parameter β has a smaller influence the more agents are in the corridor.
Finally, we estimate the two parameters β and p_{ex} using a discrete search in the range $[0.5, 10] \times [0.55, 1.65]$. In doing so we see that the outflow parameter p_{ex} can be clearly estimated for a fixed value of β, see Figure 6b. However, the parameter β is much more difficult to determine, as Figure 6a shows. Using the three data sets stated in Table 1 we obtain the best fit using

$$(\beta^{\min}, p_{ex}^{\min}) \simeq (3.84, 1.15) , \tag{5}$$

which leads to a deviation of 1.04 seconds in Equation (4). With a similar approach we then estimate the parameter $\mu_0 \simeq -1.22$ for less motivated agents according to Table 1. This results in a speed of $0.57\frac{m}{s}$.

3.3. **Microscopic simulations.** We conclude this section by presenting calibrated CA simulations, that are consistent with the experimental data. We observe that wider corridors lead to a higher maximum density in front of the exit for different motivation levels, see Figure 7b. Note that this also the case when changing the outflow rate p_{ex}. Higher motivation levels μ lead to higher densities in front of the exit as can be seen in Figure 8b.

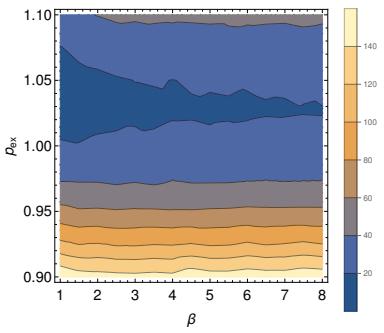

(A) The average exit time for a discrete set of β/p_{ex}-combinations.

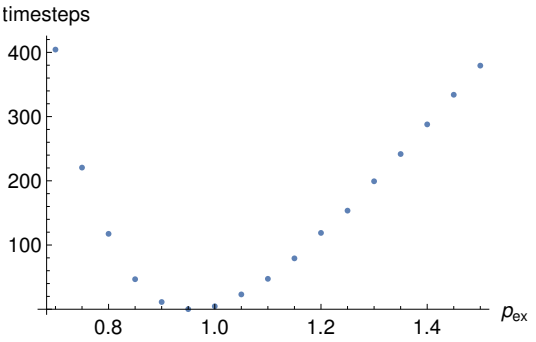

(B) $\bar{T}$ as a function of p_{ex} for a fixed value of β.

FIGURE 6. Average exit time as a function of β and p_{ex}, or p_{ex} only.

A similar behavior was observed in the experimental results as well as the computational experiments discussed in [3, 15].

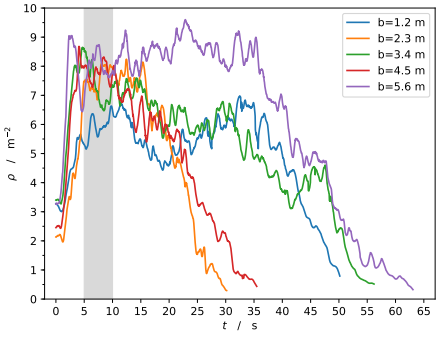

(A) Experimental results, reproduced with permission from [3].

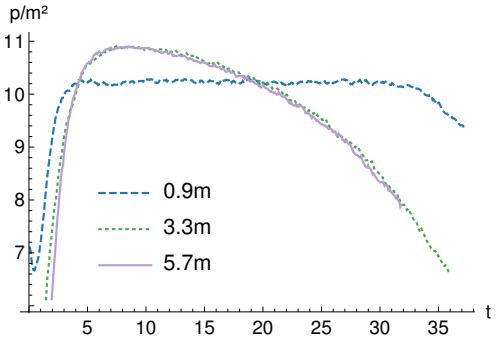

(B) Microscopic simulations for the densities for $n = 60$ and $\mu = 1$.

FIGURE 7. Impact of the corridor width on the maximum density. The CA approach yields comparable results for high density regimes and low motivation level.

Remark 3.1. Note that we observe similar results if we replace the exponential function in (1) by $\max(0, \phi(x,y) - \phi(x+\Delta x, y))$. However this function does not satisfy the necessary regularity to at least formally derive the corresponding macroscopic PDE model.

4. THE MACROSCOPIC MODEL

In this section we derived and study the corresponding macroscopic PDE model, in particular existence of solutions as well as different options to calculate the path to the exit. The corresponding macroscopic PDE can be formally derived from the cellular automaton approach discussed in Section 2.2. Here we use a Taylor expansion to develop the transition rates and functions in $x \pm \Delta x$ and $y \pm \Delta x$. This rather tedious calculation can be done in a systematic manner using a similar approach as discussed in [21].

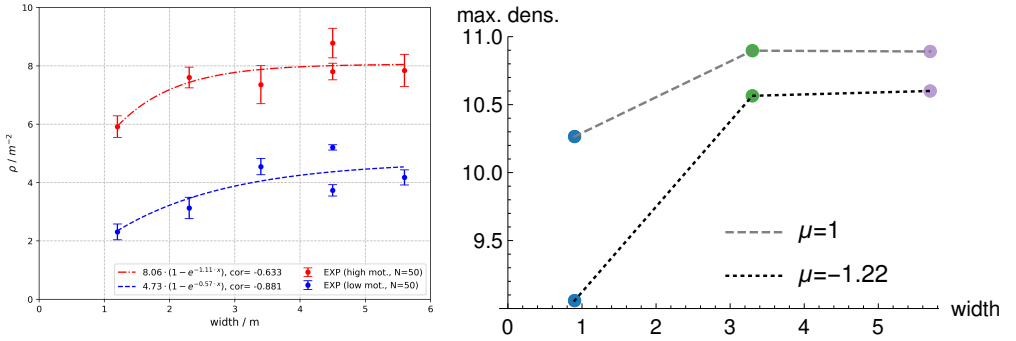

(A) Experimental results (with permission from [15])

(B) Maximum agent density using the CA model with $n = 60$.

FIGURE 8. Impact of the motivation level on the maximum pedestrian density: experimental (left) vs. microscopic simulations (right).

4.1. **The PDE and its analysis.** We recall that $\rho = \rho(x, y, t)$ denotes the density of pedestrians at position (x, y) and time t and $\phi = \phi(x, y)$ is the potential leading towards the exit Γ_E. Let $\Omega \subset \mathbb{R}^2$ denote the domain, Γ_W the walls and Γ_E the exit with $\Gamma_W \cup \Gamma_E = \partial\Omega$ and $\Gamma_W \cap \Gamma_E = \emptyset$.
Then the pedestrian density $\rho = \rho(x, y, t)$ satisfies a nonlinear Fokker-Planck equation for all $(x, y) \in \Omega$:

$$\partial_t \rho(x, y, t) = \alpha_\mu \operatorname{div} \left(\nabla \rho(x, y, t) + 2\beta \rho(x, y, t)(1 - \rho(x, y, t))\nabla \phi(x, y)\right) \tag{6a}$$

$$\rho(x, y, 0) = \rho_0(x, y). \tag{6b}$$

The parameter $\alpha_\mu := \frac{1}{8(2-\mu)}$ depends on the motivation μ, while β corresponds to the ratio between drift and diffusion. The function $\rho_0 = \rho_0(x, y)$ is the initial distribution of agents. Equation (6) is supplemented with the following boundary conditions

$$\begin{aligned} \mathbf{j} \cdot \mathbf{n} &= 0, && \text{on } \Gamma_W, \\ \mathbf{j} \cdot \mathbf{n} &= p_{ex}\rho, && \text{on } \Gamma_E, \end{aligned} \tag{6c}$$

where $\mathbf{j} = \nabla\rho + 2\beta\rho(1 - \rho)\nabla\phi$ and $\mathbf{n}$ is the unit outer normal vector. We recall that the parameter p_{ex} is the outflow rate at the exit Γ_E.

Remark 4.1. Note that the motivation parameter μ enters the PDE via α_μ only. It corresponds to a rescaling in time, accelerating or decelerating the dynamics.

First we discuss existence and uniqueness of solutions to (6). Stationary solutions of a similar model were recently investigated by Burger and Pietschmann, see [7]. The existence of the respective transient solutions was then shown in [14]. It is guaranteed under the following assumptions:

(A1) Let $\Omega \subset \mathbb{R}^2$ with boundary $\partial\Omega$ in C^2.
(A2) Let p_{ex} be in $[0, 1]$.
(A3) Let ϕ be in $H^1(\Omega)$.

Note that assumption (A1) is not satisfied in the case of a corridor. However, as pointed out in [7], this condition could be relaxed to Lipschitz boundaries with some technical effort.

Theorem 1. (Existence of weak solutions) Let assumptions (A1)-(A3) be satisfied. Let $\mathcal{S} = \{\rho \in L^2(\Omega) : 0 \le \rho \le 1\}$ and the initial datum $\rho_0 : \Omega \to \mathcal{S}^o$ be a measurable function such that $E(\rho_0) < \infty$, where entropy E is defined by

$$E(\rho) = \int_\Omega [\rho \log \rho + (1-\rho)\log(1-\rho) + 2\beta\rho\phi]\, dx\,. \tag{7}$$

Then there exists a weak solution to system (6) in the sense of

$$\int_0^T \Big[\langle \partial_t \rho, \varphi\rangle_{H^{-1},H^1} ds - \alpha_\mu \int_\Omega ((2\beta\rho(1-\rho)\nabla\phi + \nabla\rho))\nabla\varphi dx + p_{ex}\int_{\Gamma_E} \rho\varphi ds\Big] dt = 0, \tag{8}$$

for test functions $\varphi \in H^1(\Omega)$. Furthermore

$$\partial_t \rho \in L^2(0,T; H(\Omega)^{-1}),$$
$$\rho \in L^2(0,T; H^1(\Omega)).$$

The existence proof is based on the formulation of the equation in entropy variables, that is

$$\partial_t \rho(x,t) = \mathrm{div}(m(\rho)\nabla u(x,t)), \tag{9}$$

where $m(\rho) = \rho(1-\rho)$ is the mobility function and $u = \frac{\delta E}{\delta \rho} = (\log\rho - \log(1-\rho) + 2\beta\phi)$ the so-called entropy variable. Note that the proof is a straightforward adaptation of the one presented in [14], hence we omit its details in the following.

4.2. **Moving towards the exit.** In the following we discuss different possibilities to compute the potential ϕ.

The eikonal equation. The shortest path to a target, such as the exit Γ_E can be computed by solving the eikonal equation

$$\begin{aligned} \|\nabla \phi_E(x,y)\|^2 &= 1, && \text{for } (x,y) \text{ in } \Omega,\\ \phi_E(x,y) &= 0, && \text{on } (x,y) \text{ in } \Gamma_E. \end{aligned} \tag{10}$$

Solutions to (10) are in general bounded and continuous, but not differentiable, see [5]. However, in case of the considered corridor geometry we have the following improved regularity result.

Theorem 2. (Regularity of ϕ_E) Let $\Omega \subset \mathbb{R}^2$ be a rectangular domain and $\Gamma_E \subset \partial\Omega$ be a line segment in one of the four edges. Then there exists a solution $\phi_E \in H^1(\Omega)$ to (10).

The proof can be found in the Appendix and is based on [5], Proposition 2.13.

The Laplace equation. Alternatively we consider an idea proposed by Piccoli and Tosin in [30]. Let $\phi_L = \phi(x,y)$ denote the solution of the Laplace equation on $\Omega \subset \mathbb{R}^2$:

$$\begin{aligned} \Delta\phi_L(x,y) &= 0, && \text{for } (x,y) \text{ in } \Omega,\\ \phi_L(x,y) &= d(x,y), && \text{for } (x,y) \text{ on } \partial\Omega, \end{aligned} \tag{11}$$

where $d = d(x,y)$ corresponds to the Euclidean distance of the boundary points to the exit Γ_E. Note that in this case of the corridor the function d is not differentiable at the corners but Lipschitz continuous. Hence standard methods for elliptic equations yield the following regularity result.

Theorem 3. (Regularity of ϕ_L) Let $d \in C(\partial\Omega)$ defined as above, $\Omega \subset \mathbb{R}^2$ be bounded. Then there exists a unique solution $\phi_L \in H^1(\Omega)$ to (11).

The proof can be found in [22], Section 5.
In the following we discuss the similarities and difference of the potentials ϕ_E and ϕ_L. In case of a 1D corridor with a single exit, that is a line with a single exit on one of the two endpoints, the potentials are identical. However in the case of two exits at the respective endpoints, the Laplace equation gives $\phi_L(x) = 0$, a solution that is not sensible.
Figures 9 and 10 illustrate the differences between ϕ_L and ϕ_E in 2D. Note that we choose homogeneous Neumann boundary conditions at the obstacle walls when solving the Laplace equation (11). We observe good agreement in case of convex obstacles, see Figure 9. In case of non-convex obstacles, such as the U-shaped obstacle in Figure 10, individuals would first get trapped inside the U using the Laplace equation. Solving the eikonal equation (10) is in general computationally more expensive than the Laplace equation (11). However, these costs are negligible since the potential is stationary and computed once only.

(A) Eikonal equation.

(B) Laplace equation (with Neumann bc at the obstacle).

FIGURE 9. Comparison of the potentials ϕ_E and ϕ_L for a convex obstacle.

4.3. **Characteristic calculus.** We now consider the corresponding inviscid macroscopic model, which can be derived using a different scaling limit from the CA approach. We focus on the one dimensional case only as we can calculate solutions explicitly. A similar problem (with different boundary conditions) was partially analyzed in [12].

(A) Eikonal equation.

(B) Laplace equation (with Neumann bc at the obstacle).

FIGURE 10. Comparison of the potentials ϕ_E and ϕ_L for a non-convex obstacle.

The inviscid PDE reduces to a scalar conservation law, posed on $\mathbb{R}_+$ of the form

$$\partial_t \rho + \partial_x j(\rho) = 0\,, \tag{12}$$

where the flux function is $j(\rho) = -\rho(1-\rho)$. Note that this flux corresponds to the potential $\phi(x) = x$, hence individuals move to the left. We consider the initial condition

$$\rho(x,0) = \rho_0\, \chi_{[0,L]}\,,$$

for some positive L, where χ denotes the characteristic function. At the origin, we wish to enforce a similar outflow condition as in the viscid case and set $j(0,t) = p_{ex}\,\rho,\ t > 0$. This is equivalent to the Dirichlet boundary condition $\rho(0,t) = 1 - p_{ex}$ for all times $t > 0$, where we recall that $0 < p_{ex} \leq 1$. This is an ill-posed problem in general [26], and the boundary condition must be relaxed.
Away from discontinuities, the speed of characteristics is given by

$$j'(\rho) = -(1-2\rho)\,.$$

We see that they either point in- or outside of the domain, depending on the magnitude of ρ. Recall that for a shock located at $s(t)$, the Rankine-Hugoniot condition reads $[\![j'(\rho)]\!] = \dot{s}(t)[\![\rho]\!]$, where $[\![f]\!] = f^- - f^+$, with $f^\pm(x) = f(x \pm 0)$. For our choice for ρ_0, there is an initial shock at $x_r = L$, which is moving (left) at a speed of

$$\dot{x}_r = -(1-\rho_0)\,.$$

The larger the initial pedestrian density, the slower the shock moves or the people get closer to the exit. One can easily check that such a profile satisfies the so-called Lax entropy condition, since

$$-1 = j'(0) \leq \dot{x}_r \leq j'(\rho_0)\,,$$

is it therefore admissible.
Next we discuss the behavior of solutions at the exit $x = 0$. The proper way to enforce the Dirichlet boundary condition is derived in [24, 23], and reads as follows:

$$\rho^+(0) \in \mathcal{E}[1-p_{ex}] := \begin{cases} [0, p_{ex}] \cup \{1-p_{ex}\} & \text{if } p_{ex} < \tfrac{1}{2}\,, \\ [0, \tfrac{1}{2}] & \text{if } p_{ex} \geq \tfrac{1}{2}\,. \end{cases} \tag{13}$$

Depending on the slope of the characteristics as well as the value of the outflow rate p_{ex}, we observe three different cases, which are detailed below and illustrated in Figure 11.

- A constant profile for $\rho_0 \leq p_{ex} < \frac{1}{2}$ or $\rho_0 \leq \frac{1}{2} \leq p_{ex}$. In this case the characteristics have a negative slope and ρ_0 is an admissible boundary value. The function ρ vanishes when the shock originating at $x = L$ reaches the origin at time $t = \frac{L}{1-\rho_0}$. The situation is similar in the case $\frac{1}{2} < \rho_0 = 1 - p_{ex}$, for which characteristics are going inwards but where $\rho_0 \in \mathcal{E}[1-p_{ex}]$. This case is illustrated on the lower right in Figure 11.

- A shock originating at $x = 0$ for $p_{ex} < \frac{1}{2}$ and $p_{ex} < \rho_0 < 1 - p_{ex}$. In this case $\rho_0 \notin \mathcal{E}[1-p_{ex}]$, but $1 - p_{ex} \in \mathcal{E}[1-p_{ex}]$ which we therefore set as a boundary value. This causes a shock at the origin, which travels to the right with speed

  $$\dot{x}_l = \frac{-p_{ex}\,(1-p_{ex}) + \rho_0\,(1-\rho_0)}{1 - p_{ex} - \rho_0}\,,$$

  until it collides with the back-shock. The collision time and position, $t = t_1^*$ and $x = x_1^*$ respectively, can be calculated from $x_1^* = \dot{x}_l t_1^* = L + \dot{x}_r t_1^*$. We obtain

  $$t_1^* = \frac{L}{1-p_{ex}}\,, \quad \text{and} \quad x_1^* = \left(1 - \frac{1-\rho_0}{1-p_{ex}}\right) L\,.$$

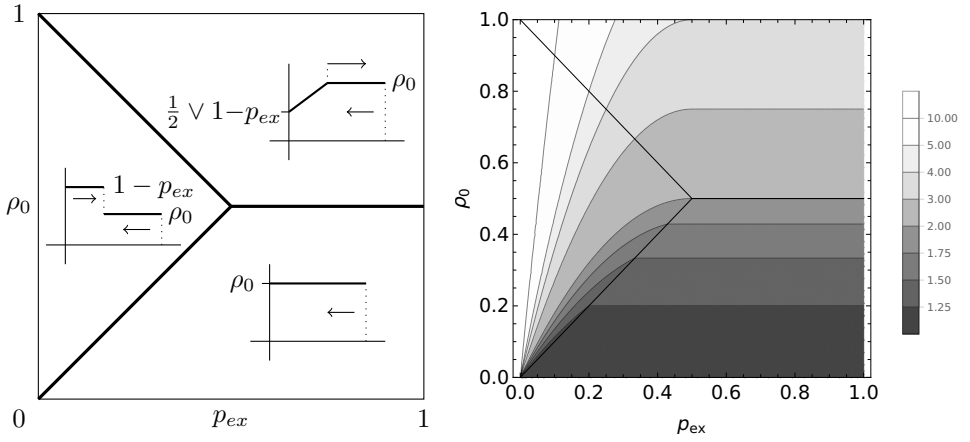

FIGURE 11. Left: Bifurcation diagram detailing the behavior of the solution to (12)-(13). The behavior along the interface lines is identical as in the bottom right corner. Right: exit time corresponding to $L = 1$.

The resulting shock will then move to the left again, with speed $-p_{ex}$ and reaches the origin at time $t = \frac{\rho_0 L}{p_{ex}(1-p_{ex})}$. This situation is shown in the center left part of Figure 11.

- A rarefaction wave originating at $x = 0$ for $\rho_0 > \frac{1}{2}$ or $\rho_0 > 1 - p_{ex}$. In this case a rarefaction wave will connect the value at the boundary, that is $\bar\rho = \frac{1}{2} \vee 1 - p_{ex}$, with the state ρ_0. The rarefaction wave is of the form $\rho(x,t) = \frac{x+t}{2t}$. More precisely we have for any $x > 0$:

$$\rho(x,t) = \begin{cases} \bar\rho & \text{if } \frac{x}{t} \le (2\bar\rho - 1) \ , \\ \frac{x+t}{2t} & \text{if } (2\bar\rho - 1) < \frac{x}{t} < (2\rho_0 - 1) \ , \\ \rho_0 & \text{if } \frac{x}{t} \ge (2\rho_0 - 1) \ . \end{cases} \tag{14}$$

Note that for $1 - p_{ex} > \frac{1}{2}$, the constant value $\bar\rho = 1 - p_{ex}$ is transported into the domain at speed $2\bar\rho - 1$. The crest the rarefaction wave travels at speed $2\rho_0 - 1$ until it hits the back-shock at time $t_2^* = \frac{L}{\rho_0}$, for $x_2^* = \left(\frac{2\rho_0 - 1}{\rho_0}\right) L$. This results at a new shock, which originates at position x_s and with velocity $\dot x_s = -(1 - \rho(x_s))$. From (14) we also have $\rho(x_s) = \frac{x_s+t}{2t}$. Solving the resulting equation with initial condition $x_s(t_2^*) = x_2^*$ yields

$$x_s(t) = 2\sqrt{L\,\rho_0}\sqrt{t} - t \, .$$

If $1 - p_{ex} < \frac{1}{2}$, this new shock reaches 0 at time $t_3^* = 4\rho_0 L$. Otherwise, the back-shock will meet the constant state $1 - p_{ex}$ at time $t_4^* = \frac{L\rho_0}{(1-p_{ex})^2}$, for $x_4^* = \frac{L(1-2p_{ex})\rho_0}{(1-p_{ex})^2}$, resulting in a single constant state $\rho(x, t_4^*) = (1 - p_{ex})\chi_{[0,x_4^*]}$. This constant profile then moves with speed $-p_{ex}$, and reaches the origin at time $t = \frac{\rho_0 L}{p_{ex}(1-p_{ex})}$, see upper right corner of Figure 11.

Figure 11 illustrates how the exit time changes with the initial pedestrian density and the outflow rate. We see that for an outflow rate $p_{ex} \gtrsim \frac{1}{2}$, the initial density ρ_0 has a much stronger influence on the exit time compared to the value of p_{ex}. The situation is somehow reversed for small p_{ex}.

4.4. **Numerical results.** We conclude by presenting computational results on the macroscopic level. All simulations were performed using the finite element library Netgen/-NgSolve.
We consider a rectangular domain with a single exit as shown in Figure 1a and discretize it using a triangular mesh of maximum size $h = 0.1$. The potential ϕ is calculated in a preliminary step, by either solving the eikonal equation (10) or the Laplace equation (11). We use a fast sweeping scheme for the eikonal equation, as it can be generalized to triangular meshes, see [31]. The discretization of the nonlinear Fokker-Planck equation (6) is based on a 4^{th} order Runge-Kutta method in time and a hybrid discontinuous Galerkin method in space, see [25].
We choose a constant initial datum ρ_0, taken such that $\int_\Omega \rho_0 dx = \frac{n}{\rho_s}$. We recall that ρ_s corresponds to the typical pedestrian density $\rho_s = 11.11 \frac{p}{m^2}$ and n to the number of individuals. The simulation parameters are set to

$$\beta = 3.84,\ p_{ex} = 1.15,\ \Delta t = 10^{-5},\ \text{and } \alpha_\mu = 1.6 \times 10^{-4}.$$

We calculate the densities in the rectangular area highlighted in Figure 1b. The macroscopic simulations confirm the microscopic results. Again higher densities for wider corridors are observed, see Figure 12a.

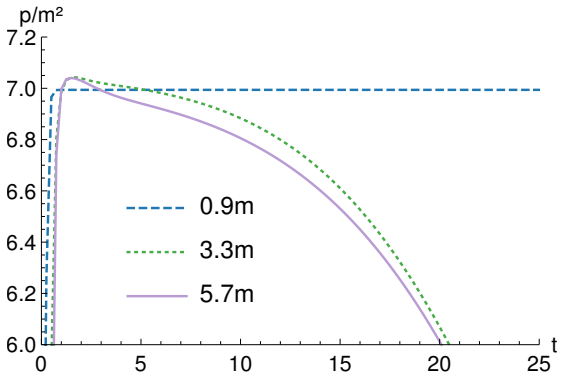

(A) For $n = 60$, the effect of higher densities for wider corridors also occur on a macroscopic scale.

5. Alternative modeling approaches

We have seen that the proposed CA approach proposed in Section 2.2 reproduces some features of the observed dynamics on the microscopic as well as on the macroscopic level. In the following, we discuss possible alternatives and generalizations, which we expect to result in even more realistic results.

5.1. **Density dependent cost.** Hughes [17] proposed that the cost of moving should be proportional to the local pedestrian density. In particular, moving through regions of high density is more expensive and therefore less preferential. This corresponds to a density dependent (hence time dependent) right-hand side in (10). In particular, Hughes proposed a coupling via

$$\begin{aligned} \|\nabla\phi(x,y,t)\| &= \frac{1}{1-\rho(x,y,t)}, && \text{for } (x,y) \text{ in } \Omega \\ \phi(x,y) &= 0, && \text{for } (x,y) \text{ in } \Gamma_E. \end{aligned} \tag{15}$$

We see that the right hand side, which corresponds to the cost of moving, becomes unbounded as ρ approaches the scaled maximum density 1. Such density dependent cost should lead to more realistic dynamics. However the analysis of the coupled problem (6)-(15) is open. Solutions to (15) have a much lower regularity required in Theorem 2. We expect that this leads to similar analytic challenges as reported in [12].

5.2. **Alternative ways to model motivation.** In the following, we discuss different possibilities to include the influence of the motivation level on the dynamics. First by modifying the transition rates and second by changing the transition mechanism, allowing for shoving.

Alternative transition rates. In the transition rate (1), the motivation relates to the probability of jumping. It is therefore directly correlated to the agent's velocity. However, one could assume that the motivation increases the probability to move along the shortest path. This could be modeled by transition rates of the form

$$\mathcal{T}^{+0}(x,y) = (1-\rho(x+\Delta x,y,t))\frac{1}{8}\exp(\mu\beta(\phi(x,y)-\phi(x+\Delta x,y))). \tag{16}$$

Then the corresponding macroscopic model reads

$$\partial_t\rho(x,y,t) = \frac{1}{8}\operatorname{div}\left(\nabla\rho(x,y,t) + 2\mu\beta\rho(x,y,t)(1-\rho(x,y,t))\nabla\phi(x,y)\right). \tag{17}$$

We see that the motivation level μ enters only in the convective term. Hence higher motivation is directly correlated to a higher average velocity of the crowd.

Pushing and shoving. In the previously proposed model, the transition rates depended on the availability of a site and the motivation level. Another possibility to include the latter is by allowing individuals to push. Different pushing mechanisms have been proposed in the literature. However, not all of them can be transposed to bounded domains. In particular, it is not clear how to adapt boundary conditions in case of global pushing, as considered in [4]. In contrast, local pushing mechanisms, can be translated one-to-one on bounded domains, see [38]. We sketch the rough idea in 1D: with a given probability, agents can move to a neighboring occupied cell, by pushing the neighbor one cell further, provided that it is free. Otherwise, such a move is forbidden. This mechanism is illustrated in Figure 13.

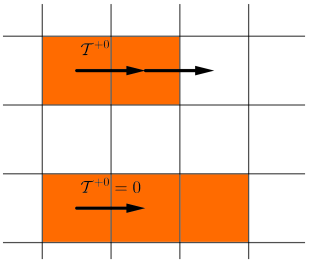

FIGURE 13. Local pushing in a cellular automaton. Top: shoving is possible since the cell on the third column in free. Bottom: shoving is forbidden since the third column is occupied.

Superscripts ± 1 denote jumps to the right and left, respectively. For example

$$\mathcal{T}^{+}(x) = \exp(\beta(\phi(x)-\phi(x+\Delta x))).$$

Then the master equation is given by

$$
\begin{aligned}
\rho(x,t+\Delta t)-\rho(x,t) = &-\rho(x)\mathcal{T}^+(x)\left((1-\rho(x+\Delta x))+\gamma_\mu\rho(x+\Delta x)(1-\rho(x+2\Delta x))\right)\\
&-\rho(x)\mathcal{T}^-(x)\left((1-\rho(x-\Delta x))+\gamma_\mu\rho(x-\Delta x)(1-\rho(x-2\Delta x))\right)\\
&+\rho(x+\Delta x)\mathcal{T}^-(x+\Delta x)(1-\rho(x))\\
&+\gamma_\mu\rho(x+\Delta x)\rho(x+2\Delta x)\mathcal{T}^-(x+2\Delta x)(1-\rho(x))\\
&+\rho(x-\Delta x)\mathcal{T}^+(x-\Delta x)(1-\rho(x))\\
&+\gamma_\mu\rho(x-\Delta x)\rho(x-2\Delta x)\mathcal{T}^+(x-2\Delta x)(1-\rho(x))\,,
\end{aligned}
\tag{18}
$$

in which we omit x and t for the sake of readability. Here $\gamma_\mu = \gamma(\mu) \in [0,1]$ denotes an increasing function and corresponds to the probability of an agent pushing. Note that we obtain the original master equation (2) for $\gamma_\mu = 0$. Using a formal Taylor expansion we derive the limiting mean-field PDE:

$$
\begin{aligned}
\partial_t\rho(x,y,t) &= \alpha_\mu \operatorname{div}\big((1+4\gamma_\mu\rho)\nabla\rho + 2\beta\rho(1-\rho)(1+2\gamma_\mu\rho)\nabla\phi\big)\\
\rho(0,x) &= \rho_0(x,y).
\end{aligned}
\tag{19}
$$

This equation has again a formal gradient flow structure with respect to the Wasserstein metric. In particular, a possible choice of mobility and entropy are $m(\rho) = \rho(1-\rho)(1+2\gamma_\mu\rho)$ and

$$
\begin{aligned}
E(\rho) = \int_\Omega \Big[&\frac{4\gamma+1}{2\gamma+1}(1-\rho)\log(1-\rho)\\
&+\rho\log\rho+\frac{2\gamma\rho+1}{2\gamma+1}\log(2\gamma\rho+1)+2\beta\rho\phi\Big]\,dx\,,
\end{aligned}
\tag{20}
$$

respectively. We observe that the local pushing increases the mobility and adds a positive term to the entropy. Hence we expect a faster equilibration speed compared to the model of Section 4.1. Again, we recover the original PDE model by setting $\gamma_{mu} = 0$. Existence of global in time solutions to (19) should follow using similar arguments as for the original PDE model.

6. Conclusion

In this paper we discussed micro- and macroscopic models for crowding and queuing at exits and bottlenecks, which were motivated by experiments conducted at the University in Wuppertal. These experiments indicated that the geometry, ranging from corridors to open rooms, as well as the motivation level, such as a higher incentive to get to the exit due to rewards, changes the overall dynamics significantly.
We propose a cellular automaton approach, in which the individual transition rates increase with the motivation level, and derive the corresponding continuum description using a formal Taylor expansion. We use experimental data to calibrate the model and to understand the influence of parameters and geometry on the overall dynamics. Both the micro- and the macroscopic description reproduce the experimental behavior correctly. In particular we observe that corridors lead to lower densities and that the geometry has a stronger effect than the motivation level. We plan to investigate the analysis of the coupled Hughes type models as well as the dynamics in case of pushing in more detail in the future.

Acknowledgments

The authors would like to thank Christoph Koutschan for the helpful discussions and input concerning the derivation of the respective mean field models using symbolic techniques. Furthermore we would like to thank the team at the Forschungszentrum Jülich

and the University of Wuppertal, in particular Armin Seyfried and Ben Hein, for providing the data and patiently answering all out questions.
All authors acknowledges partial support from the Austrian Academy of Sciences via the New Frontier's grant NST 0001 and the EPSRC by the grant EP/P01240X/1.

References

[1] Crowding and queuing at entrances, 2018 (accessed February 3, 2019). http://ped.fz-juelich.de/da/doku.php?id=wuptmp. 2.1, 3.2
[2] Jupedsim, 2019 (accessed Juni 5, 2019). https://www.jupedsim.org. 2.1
[3] J. Adrian, M. Boltes, S. Holl, A. Sieben, and A. Seyfried. Crowding and Queuing in Entrance Scenarios: Influence of Corridor Width in Front of Bottlenecks. arXiv e-prints, page arXiv:1810.07424, Oct 2018. 1, 2.1, 1, 3.3, 7a
[4] A. Almet, M. Pan, B. Hughes, and K. Landman. When push comes to shove: Exclusion processes with nonlocal consequences. Physica A: Statistical Mechanics and its Applications, 437, 05 2015. 5.2
[5] M. Bardi and I. Capuzzo-Dolcetta. Optimal Control and Viscosity Solutions of Hamilton-Jacobi-Bellman Equations. Modern Birkhäuser Classics. Birkhäuser Boston, 2008. 4.2, 4.2, 7
[6] M. Burger, S. Hittmeir, H. Ranetbauer, and M.-T. Wolfram. Lane formation by side-stepping. SIAM Journal on Mathematical Analysis, 48, 07 2015. 1
[7] M. Burger and J.-F. Pietschmann. Flow characteristics in a crowded transport model. Nonlinearity, 29(11):3528, Nov 2016. 1, 4.1, 4.1
[8] C. Burstedde, K. Klauck, A. Schadschneider, and J. Zittartz. Simulation of pedestrian dynamics using a two-dimensional cellular automaton. Physica A: Statistical Mechanics and its Applications, 295:507–525, 06 2001. 2.2
[9] L. Caffarelli and M. Crandall. Distance functions and almost global solutions of eikonal equations. Communications in Partial Differential Equations, 35:391–414, 03 2010. 7
[10] A. Corbetta, J. A. Meeusen, C.-m. Lee, R. Benzi, and F. Toschi. Physics-based modeling and data representation of pairwise interactions among pedestrians. Physical Review E, 98:062310, Dec 2018. 1
[11] E. Cristiani, B. Piccoli, and A. Tosin. Multiscale Modeling of Pedestrian Dynamics, volume 12. 10 2014. 1
[12] M. Di Francesco, P. Markowich, J.-F. Pietschmann, and M.-T. Wolfram. On the Hughes' model for pedestrian flow: the one-dimensional case. Journal of Differential Equations, 250(3):1334–1362, 2 2011. 1, 4.3, 5.1
[13] D. C. Duives, W. Daamen, and S. Hoogendoorn. Trajectory analysis of pedestrian crowd movements at a Dutch music festival. In Pedestrian and Evacuation Dynamics 2012, pages 151–166. Springer, 2014. 3.2
[14] S. N. Gomes, A. M. Stuart, and M.-T. Wolfram. Parameter estimation for macroscopic pedestrian dynamics models from microscopic data. SIAM Journal on Applied Mathematics, 79(4):1475–1500, 2019. 1, 4.1, 4.1
[15] B. Hein. Agent-based modelling for crowding and queuing in front of bottlenecks. Bachelor's thesis, University of Wuppertal, 2019. 2.2, 3.2, 3.3, 8a
[16] D. Helbing and P. Molnar. Social force model for pedestrian dynamics. Physical Review E, 51(5):4282, 1995. 1
[17] R. Hughes. A continuum theory for the flow of pedestrians. Transportation Research Part B: Methodological, 36:507–535, 07 2002. 1, 5.1
[18] A. Johansson and D. Helbing. Analysis of empirical trajectory data of pedestrians. Pedestrian and Evacuation Dynamics 2008, pages 203–214, 12 2010. 1
[19] A. Jüngel. The boundedness-by-entropy method for cross-diffusion systems. Nonlinearity, 28(6):1963, 2015. 1
[20] A. Kirchner and A. Schadschneider. Simulation of evacuation processes using a bionics-inspired cellular automaton model for pedestrian dynamics. Physica A: Statistical Mechanics and its Applications, 312:260–276, 09 2002. 1, 2.2
[21] C. Koutschan, H. Ranetbauer, G. Regensburger, and M.-T. Wolfram. Symbolic derivation of mean-field pdes from lattice-based models. 2015 17th International Symposium on Symbolic and Numeric Algorithms for Scientific Computing (SYNASC), pages 27–33, 2015. 1, 4
[22] O. Ladyzhenskaya. Linear and Quasilinear Elliptic Equations. ISSN. Elsevier Science, 1968. 4.2

[23] P. LeFloch. Explicit formula for scalar nonlinear conservation laws with boundary condition. Mathematical Methods in the Applied Sciences, 10(3):265–287, 1988. 4.3
[24] P. LeFloch and J.-C. Nédélec. Explicit formula for weighted scalar nonlinear hyperbolic conservation laws. Transactions of the American Mathematical Society, 308(2):667–683, 1988. 4.3
[25] C. Lehrenfeld. Hybrid Discontinuous Galerkin methods for solving incompressible flow problems. PhD thesis, 05 2010. 4.4
[26] A. Y. Leroux. Approximation de quelques problèmes hyperboliques non-linéaires. Thèse d'état, Rennes, 1979. 4.3
[27] B. Maury and S. Faure. Crowds in Equations, volume 1. 09 2018. 1
[28] M. Moussaïd, D. Helbing, S. Garnier, A. Johansson, M. Combe, and G. Theraulaz. Experimental study of the behavioural mechanisms underlying self-organization in human crowds. Proceedings. Biological sciences / The Royal Society, 276:2755–62, 06 2009. 1
[29] S. Nowak and A. Schadschneider. Quantitative analysis of pedestrian counterflow in a cellular automaton model. Physical Review E, 85, 06 2012. 1, 2.1
[30] B. Piccoli and A. Tosin. Time-evolving measures and macroscopic modeling of pedestrian flow. Archive for Rational Mechanics and Analysis, 199(3):707–738, Mar 2011. 1, 4.2
[31] J. Qian, Y.-T. Zhang, and H.-K. Zhao. Fast sweeping methods for eikonal equations on triangular meshes. SIAM J. Numerical Analysis, 45:83–107, 01 2007. 4.4
[32] C. Rudloff, T. Matyus, and S. Seer. Comparison of different calibration techniques on simulated data. In Pedestrian and Evacuation Dynamics 2012, pages 657–672. Springer, 2014. 3.2
[33] A. Schadschneider, C. Eilhardt, S. Nowak, and R. Will. Towards a calibration of the floor field cellular automaton. Pedestrian and Evacuation Dynamics, pages 557–566, 01 2011. 1
[34] A. Schadschneider, H. Klüpfel, T. Kretz, C. Rogsch, and A. Seyfried. Fundamentals of Pedestrian and Evacuation Dynamics, pages 124–154. 06 2009. 1
[35] M. Twarogowska, P. Goatin, and R. Duvigneau. Comparative study of macroscopic pedestrian models. Transportation Research Procedia, 2, 12 2014. 1
[36] U. Weidmann. Transporttechnik der Fussgänger: transporttechnische Eigenschaften des Fussgängerverkehrs. Schriftenreihe des IVT. IVT, 1993. 3.2
[37] W. Weng, T. Chen, H. Yuan, and W. Fan. Cellular automaton simulation of pedestrian counter flow with different walk velocities. Physical Review. E, 74:036102, 10 2006. 2.1, 3.2
[38] C. Yates, A. Parker, and R. Baker. Incorporating pushing in exclusion-process models of cell migration. Physical Review E, 91, 04 2015. 5.2

7. Appendix

Proof 1 of Theorem 2. We start by a recalling a standard existence and regularity result from the literature, see [5] and [9]. Solutions to the eikonal equation (10) in $\mathbb{R}^2 \setminus \Gamma_E$ are given by the distance function

$$d(x, \Gamma_E) = \inf_{b \in \Gamma_E} |x - b|.$$

Hence we discuss the regularity of d in the following only. can therefore transfer our considerations to the distance function d. We define the set

$$M(x) = \arg\min_{b \in \Gamma_E} d(x, \Gamma_E).$$

If Γ_E is a straight, bounded line, the M is nonempty and consists of a single point for every $x \in \mathbb{R}^2$. Since $|(\cdot - b)|$ is uniformly differentiable in b, and $b \mapsto D_x|x - b|$ is continuous, we can deduce that the set Y

$$Y(x) := \{D_x|x - b| : b \in M(x)\}$$

is a singleton too. We now can apply Proposition 2.13 in [5] which states that d is differentiable at x if and only if $Y(x)$ is a singleton. Thus d is differentiable for $\mathbb{R}^2 \setminus \Gamma_E$, to be more precisely, we have $d \in C^1(\mathbb{R}^2 \setminus \Gamma_E) \cap C(\mathbb{R}^2)$.
Next we restrict d to the corridor $\Omega \subset \mathbb{R}^2$ (being an open and bounded subset of Ω). Hence, $\phi_E \in C(\bar{\Omega}) \cap C^1(\Omega)$. Since the L^2-norm of the first derivative of ϕ_E is bounded by

the equation (10) itself, we can deduce that $\phi_E \in H^1(\Omega)$ since

$$\|\phi_E\|_{H^1(\Omega)} = \int_\Omega \phi_E^2 dx + \int_\Omega (D\phi_E)^2 dx \leq |\Omega|(\max \phi_E + 1).$$

Radon Institute for Applied and Computational Mathematics, Altenbergerstr. 69, 4040 Linz, Austria
Email address: tbc

Radon Institute for Applied and Computational Mathematics, Altenbergerstr. 69, 4040 Linz, Austria

University of Warwick, Mathematics Institute, Gibbet Hill Road, CV47AL Coventry, UK and Radon Institute for Applied and Computational Mathematics, Altenbergerstr. 69, 4040 Linz, Austria